Opto-Electronic Science

Phonon-assisted absorption photoconductive switch

Zhao Wang, Lixin Zhang, Lu Cheng, Danwen Zhang, Yu Lu, Naiji Zhang, Xin Zhang, Duanyang Chen, Zhan Sui, Hongji Qi* and Wei Zheng*

https://doi.org/10.29026/oes.2026.260011



Opto-Electronic Science

CN 51-1800/O4 ISSN (Print) 2097-0382 ISSN (Online) 2097-4000

Phonon-assisted absorption photoconductive switch

Zhao Wang, Lixin Zhang, Lu Cheng, Danwen Zhang, Yu Lu, Naiji Zhang, Xin Zhang, Duanyang Chen, Zhan Sui, Hongji Qi* and Wei Zheng*

Citation: Wang Z, Zhang LX, Cheng L et al. Phonon-assisted absorption photoconductive switch. *Opto-Electron Sci* **5**, 260011 (2026).

https://doi.org/10.29026/oes.2026.260011

Received: 12 March 2026; Accepted: 29 April 2026; Published online: 20 May 2026

Related articles

Emerging low-dimensional perovskite resistive switching memristors: from fundamentals to devices

Shuanglong Wang, Hong Lian, Haifeng Ling et al

Opto-Electronic Advances 2025, **8**(8): 240316 doi: 10.29026/oea.2025.240316

Recent advances in exciton-polariton in perovskite

Khalil As'ham, Andergachew Mekonnen Berhe, Ibrahim A. M. Al-Ani et al

Opto-Electronic Science 2025, **4**(9): 250001 doi: 10.29026/oes.2025.250001

Active tuning of anisotropic phonon polaritons in natural van der Waals crystals with negative permittivity substrates and its application in energy transport

Shuo Chen, Xiaohu Wu, Ceji Fu

Opto-Electronic Science 2024, **3**(6): 240002 doi: 10.29026/oes.2024.240002

On-chip light control of semiconductor optoelectronic devices using integrated metasurfaces

Cheng-Long Zheng, Pei-Nan Ni, Yi-Yang Xie et al

Opto-Electronic Advances 2025, **8**(1): 240159 doi: 10.29026/oea.2025.240159

More related articles in Opto-Electronic Journals Group website

Opto-Electronic Journals Group

https://www.oejournal.org

OE_Journal

@OptoElectronAdv

OES | Opto-Electronic Science

Article

May 2026, Vol. 5, No. 5

Open Access

Phonon-assisted absorption photoconductive switch

Zhao Wang[1], Lixin Zhang[1], Lu Cheng[1], Danwen Zhang[1], Yu Lu[1], Naiji Zhang[1], Xin Zhang[1], Duanyang Chen[2], Zhan Sui[3], Hongji Qi[4,5]* and Wei Zheng[1]*

Abstract: High-power microwave technology shows great promise for applications in low-altitude security systems such as countering non-cooperative unmanned aerial vehicles. However, conventional high-power photoconductive semiconductor switches (PCSSs) based on impurity absorption intrinsically fail to achieve high voltage conversion efficiency across different operating voltages, limiting their overall performance. Here, we propose a novel PCSS based on phonon-assisted absorption, which fundamentally breaks the efficiency bottleneck and enables voltage conversion efficiency close to the theoretical limit. Using gallium oxide (Ga_2O_3), we successfully fabricate this phonon-assisted Ga_2O_3 PCSS, demonstrating a voltage conversion efficiency of 90.25% at an excitation laser energy of 1.98 mJ and a bias voltage of 600 V, as well as a conversion efficiency of 98.93% and a maximum output power density of 17.7 MW/cm^2 at a bias voltage of 4000 V. This work provides a new principle and technical route for designing and fabricating high-performance high-power photoconductive switches, significantly advancing the development of high-efficiency, high-power microwave systems.

Keywords: high-power photoconductive semiconductor switch; phonon-assisted absorption; gallium oxide; high-power microwave; low-altitude security

DOI: 10.29026/oes.2026.260011 | CSTR: 32246.14.oes.2026.260011

Citation: Wang Z, Zhang LX, Cheng L et al. Phonon-assisted absorption photoconductive switch. *Opto-Electron Sci* **5**, 260011 (2026).

1 Introduction

With the rapid development of the low-altitude economy, low-altitude security issues such as the intrusion of non-cooperative unmanned aerial vehicles (UAVs), flight conflicts and route security threats have become increasingly prominent, which puts forward an urgent demand for efficient and reliable low-altitude security technologies and equipment[1–3]. High-power microwave (HPM) technology can realize interference, functional damage and even physical burnout to the electronic information systems of non-cooperative UAVs through directional electromagnetic radiation, thus effectively responding to the security threats posed by non-cooperative UAVs[4,5]. High-power photoconductive semiconductor switches (PCSSs) are the core units in HPM transmitting systems and directly affect the overall performance of the systems[6–8]. Fabricating high-power PCSSs with more compact and efficient energy release is conducive to the lightweight development of HPM transmitting systems, enabling them to be flexibly mounted on mobile platforms with strict space and weight constraints such as UAVs, and effectively responding to various sudden low-altitude security scenarios.

High-power PCSSs require high voltage withstand capacity and high voltage conversion efficiency. Traditional PCSSs mostly use gallium arsenide (GaAs) as the main material, whose theoretical breakdown electric field strength is 0.4 MV/cm[9,10]. In contrast, semiconductor materials with larger bandgaps generally exhibit higher breakdown electric field strengths[11–15]. Taking gallium oxide (Ga_2O_3), a typical ultra-wide bandgap semiconductor, as an example, its theoretical breakdown electric field strength reaches 8 MV/cm, and its voltage withstand capacity per channel distance is 20 times that of GaAs[16–19]. This means that under the same

Received: 12 March 2026

Accepted: 29 April 2026

Published online: 20 May 2026

[1]School of Materials, Sun Yat-sen University, Shenzhen 518107, China; [2]Hangzhou Fujia Gallium Technology Company Limited, Hangzhou 311400, China; [3]Shanghai Institute of Laser Plasma, China Academy of Engineering Physics, Shanghai 201899, China; [4]Advanced Laser and Optoelectronic Functional Materials Department, Shanghai Institute of Optics and Fine Mechanics, Chinese Academy of Sciences, Shanghai 201800, China; [5]Shanghai Key Laboratory of Wide and Ultra-Wide Bandgap Semiconductor Materials, Shanghai 201306, China.

*Correspondence: HJ Qi, E-mail: qhj@siom.ac.cn; W Zheng, E-mail: zhengw37@mail.sysu.edu.cn

voltage conversion efficiency and device cross-sectional area, Ga_2O_3-based PCSSs are expected to achieve the same intensity of signal output with 1/20 the volume of GaAs-based PCSSs. In addition, Ga_2O_3 also has the advantages of excellent temperature stability and easy growth of large-size single crystals, making it the preferred material for fabricating stable PCSSs with high output energy density[20–23]. However, the currently reported Ga_2O_3-based PCSSs mainly rely on the impurity energy levels of Ga_2O_3 to realize the excitation of carriers, which results in low voltage conversion efficiency and large resistance loss, limiting the practical application of Ga_2O_3-based PCSSs in HPM transmitting systems[24–26].

To address the above problems, this work proposes a novel operating mechanism of PCSSs based on phonon-assisted absorption, in which phonon-assisted absorption is introduced into the excitation design of Ga_2O_3 PCSSs, fundamentally eliminating the dependence of Ga_2O_3 PCSSs on impurity energy levels and enabling efficient bulk carrier excitation in the active region of the material. The Ga_2O_3 PCSS fabricated based on this mechanism exhibits a voltage conversion efficiency of 98.93%, a maximum output power density of 17.7 MW/cm^2 under an excitation laser energy of 1.98 mJ and a bias electric field of 40 kV/cm. This work not only verifies the application potential of Ga_2O_3-based PCSSs but also provides a new physical paradigm and technical route for the performance improvement of high-power PCSSs based on other material systems.

2 Results and discussion

Figure 1(a) shows the application scenario of the HPM system based on high-power PCSSs in key civil infrastructure such as airports. The system can be mounted on security UAVs and respond to the potential threats of non-cooperative UAVs to passenger planes by emitting directional HPMs to interfere with or disable the electronic systems of non-cooperative UAVs. Figure 1(b) shows the influence of the output signal amplitude of PCSSs on the microwaves output by the microwave system. The higher the power of the output signal of PCSSs, the longer the effective radiation distance of the microwaves converted by the transmitting antenna, which can more effectively respond to the security threats brought by non-cooperative UAVs, and high output power requires PCSSs to work under high bias voltage with high voltage conversion efficiency. For UAVs with strict space and weight limitations, high bias voltage means that the semiconductor material itself must have a high breakdown electric field strength. As shown in Fig. 1(c), among common semiconductor materials, ultra-wide bandgap semiconductors such as Ga_2O_3, AlN and diamond have significantly higher breakdown electric field strengths[27–30]. However, the current PCSSs based on ultra-wide bandgap semiconductor materials usually realize carrier excitation by virtue of impurity energy levels, which limits the improvement of their voltage conversion efficiency[24,31]. In contrast, this work proposes a PCSS based on the phonon-assisted absorption mechanism and successfully fabricates such a device using Ga_2O_3, achieving a high voltage conversion efficiency of up to 98.93%. A comparison of the voltage conversion efficiency of PCSSs based on ultra-wide bandgap semiconductor materials in this work and other studies is shown in Fig. 1(d)[24–26,32,33].

High-quality Fe-doped Ga_2O_3 crystals are adopted to fabricate PCSSs in this work. Figure 2(a) shows the basic characteristics of the Ga_2O_3 crystals used, where (i) is the optical photograph of the Ga_2O_3 crystal, (ii) is the X-ray diffraction rocking curve of the Ga_2O_3 crystal with a full width at half maximum (FWHM) of only 19.89 arcsec, indicating that the crystal has an extremely low dislocation density and excellent single crystal integrity, and (iii) is the high-resolution transmission electron microscopy (HRTEM) image of the Ga_2O_3 crystal. The interplanar spacings of its (001) and (200) crystal planes are 0.551 nm and 0.594 nm, respectively, which are highly consistent with the theoretical spacing values of the corresponding crystal planes of β-Ga_2O_3[34]. In addition, Fig. S1 and Fig. S2 show the X-ray diffraction (XRD) pattern of the Ga_2O_3 crystal used and Raman spectra at five different positions, respectively[34,35]. The above results indicate that the Fe-doped Ga_2O_3 crystal has a preferred growth along the [100], high crystal quality, and good consistency within the measured region, laying a solid material foundation for fabricating Ga_2O_3 PCSSs with good and stable performance.

Subsequently, the Ga_2O_3 crystal is fabricated into a Ga_2O_3 PCSS, and its output characteristics are systematically tested, with the physical image of the device shown in Fig. S3. Figure 2(b) shows the schematic diagram of the test circuit of the Ga_2O_3 PCSS and its output voltage signal when operating at a bias voltage of 4000 V (corresponding to an electric field strength of 40 kV/cm). The peak output voltage reaches 3957 V, the voltage conversion efficiency is 98.93%. The voltage conversion efficiency is calculated by the formula $\eta = V_{peak}/V_{bias}$, where η is the voltage conversion efficiency, V_{bias} is the bias voltage of the PCSS, and V_{peak} is the peak output voltage of the PCSS[26]. Figure 2(c) shows the comparison of the voltage conversion efficiency and peak output power of different Ga_2O_3 PCSSs[24–26]. It can be observed that the excitation wavelength has a significant influence on the performance of Ga_2O_3 PCSSs. In particular, the Ga_2O_3 PCSS in this work exhibits much higher voltage conversion efficiency and peak output power than other reported Ga_2O_3 PCSSs, even at a relatively low excitation energy, which benefits from the phonon-assisted absorption excitation mode realized by controlling the photon energy of the excitation light.

Then, the output voltage of the Ga_2O_3 PCSS under a wide bias voltage range of 50–4000 V at an excitation laser energy of 1.98 mJ is systematically tested, with the test results shown in Fig. S4–S15. The peak output voltage of each test

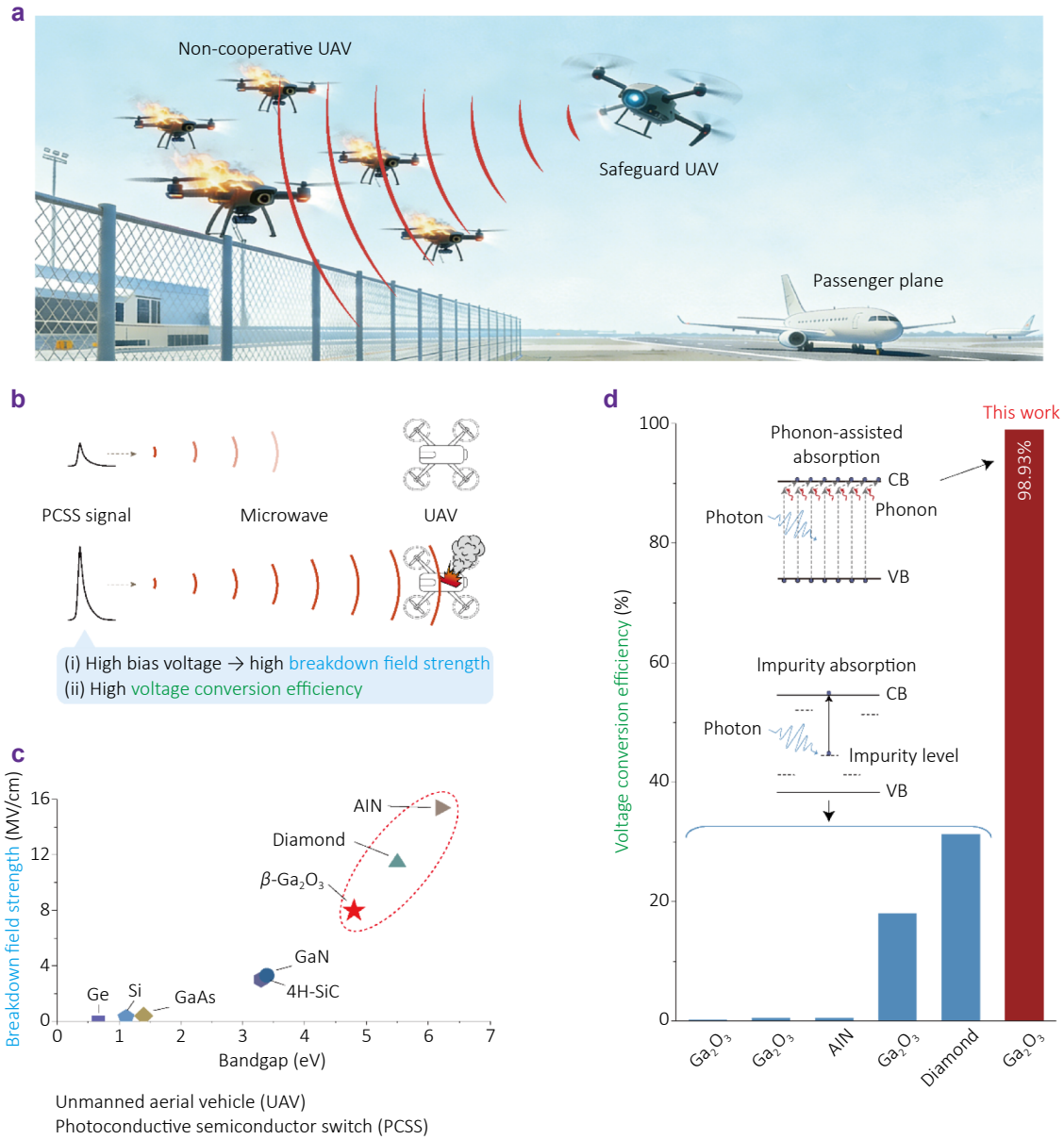


Fig. 1 | (a) Application scenario of the HPM system based on high-power PCSSs in key civil infrastructure such as airports. (b) Influence of the output signal amplitude of PCSSs on the microwaves output by the system and the basic requirements of high-power PCSSs. (c) Bandgaps and breakdown electric field strengths of different semiconductor materials. (d) Comparison of the voltage conversion efficiency of PCSSs based on ultra-wide bandgap semiconductor materials in this study and other studies[24–26,32,33].

result is extracted, and the corresponding peak output current and on-resistance are calculated by the formulas $I_{peak} = V_{peak}/R_{load}$, $P_{peak} = V_{peak} \times I_{peak}$ and $R_{on} = V_{bias}/I_{peak} - R_{load}$, where I_{peak} is the peak output current, V_{peak} is the peak output voltage, R_{load} is the load resistance, P_{peak} is the peak output power, R_{on} is the minimum on-resistance, and V_{bias} is the bias voltage of the PCSS[26,36]. Figure 2(d) shows the variation trends of the peak output voltage, voltage conversion efficiency, peak output power and minimum on-resistance with the bias voltage at an excitation laser energy of 1.98 mJ. It can be observed from Fig. 2(d) (i) that the peak output voltage of the Ga_2O_3 PCSS shows an increasing trend with the increase of the bias electric field strength, and the peak output voltage at 4000 V can reach 3957 V. The small standard deviation also indicates the output stability of the Ga_2O_3 PCSS under different operating conditions. Figure 2(d) (ii) shows that the Ga_2O_3 PCSS has a high voltage conversion efficiency over a wide bias voltage range. It has a voltage conversion efficiency of 47.49% at a bias voltage of 50 V, 90.25% at a bias voltage of 600 V, and even up to 98.93% at a bias voltage of 4000 V. Figure 2(d) (iii) shows the peak output power of the Ga_2O_3

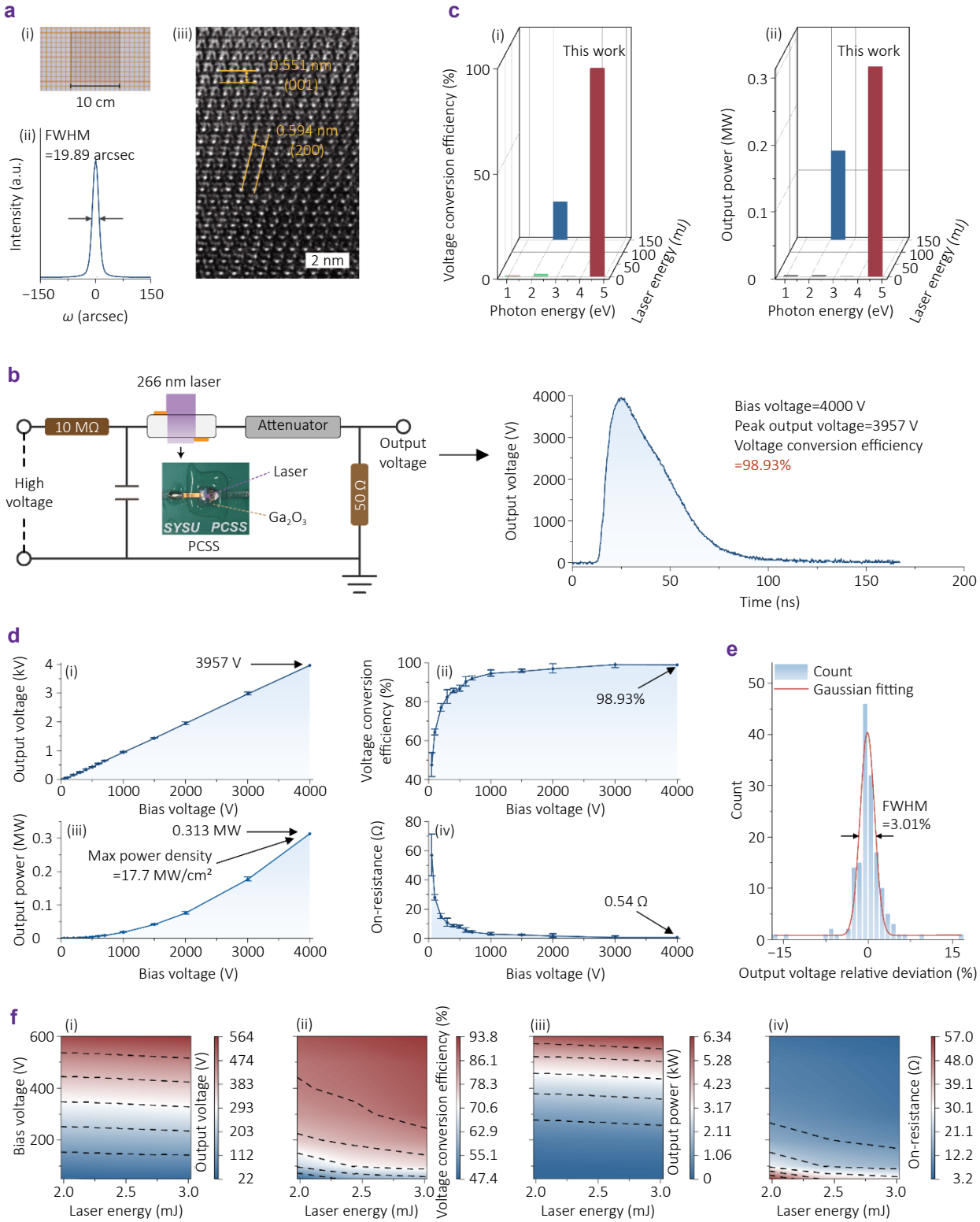


Fig. 2 | (a) Basic characteristics of the Ga_2O_3 crystal. (i) Optical photograph of the Ga_2O_3 crystal, (ii) X-ray diffraction rocking curve of the Ga_2O_3 crystal, (iii) HRTEM image of the Ga_2O_3 crystal. (b) Schematic diagram of the test circuit of the Ga_2O_3 PCSS and its output voltage signal when operating at a bias voltage of 4000 V (corresponding to an electric field strength of 40 kV/cm). (c) Comparison of (i) voltage conversion efficiency and (ii) peak output power of Ga_2O_3 PCSSs in this study and other studies[24–26]. (d) Variation trends of (i) peak output voltage, (ii) voltage conversion efficiency, (iii) peak output power and (iv) minimum on-resistance with bias voltage for the Ga_2O_3 PCSS at an excitation laser energy of 1.98 mJ. (e) Distribution of the relative deviation of the peak output voltage of the Ga_2O_3 PCSS. (f) Contour plots of peak output voltage, voltage conversion efficiency, peak output power and minimum on-resistance of the Ga_2O_3 PCSS under a bias voltage of 50~600 V at excitation laser energies of 1.98 mJ, 2.44 mJ and 3.02 mJ, respectively.

PCSS under different bias voltages. At 4000 V, it has a high peak output power of 0.313 MW, and the peak power density output by the Ga_2O_3 PCSS can be calculated to be 17.7 MW/cm^2 based on the incident spot area, which reflects its great potential in achieving high output energy density. Figure 2(d) (iv) shows the on-resistance of the Ga_2O_3 PCSS, which is only 0.54 Ω at a bias voltage of 4000 V, indicating that the Ga_2O_3 PCSS has low resistance loss during operation and can realize energy conversion effectively. Furthermore, the relative deviation of the peak output voltage of the Ga_2O_3 PCSS under the same operating condition is calculated and its distribution is statistically analyzed, with the results shown in Fig. 2(e). The results show that the relative deviation of the peak voltage conforms to the Gaussian distribution with a FWHM of only 3.01%, which further illustrates the operating stability of the Ga_2O_3 PCSS.

To determine the influence of excitation laser energy on the output characteristics of the Ga_2O_3 PCSS, Fig. 2(f) shows the contour plots of the peak output voltage, voltage conversion efficiency, peak output power and minimum on-resistance of the Ga_2O_3 PCSS under a bias voltage of 50–600 V at excitation laser energies of 1.98 mJ, 2.44 mJ and 3.02 mJ, respectively. In addition, the test results at excitation laser energies of 2.44 mJ and 3.02 mJ are shown in Figs. S16–S29, and the variation trends of various output characteristics of the Ga_2O_3 PCSS with bias voltage at different excitation laser energies are shown in Figs. S30–S33. The above results show that at the same bias voltage, the peak output voltage, voltage conversion efficiency, peak output power and minimum on-resistance of the Ga_2O_3 PCSS change slightly with the excitation laser energy, which indicates that the excitation laser energy has a small influence on the output performance of the Ga_2O_3 PCSS and that high-performance output of the Ga_2O_3 PCSS can be achieved with a small excitation laser energy.

The ability of the Ga_2O_3 PCSS to achieve high voltage conversion efficiency over a wide bias voltage range with a small excitation laser energy benefits from the construction of the PCSS based on the phonon-assisted absorption mechanism proposed in this work. Figure 3 shows the carrier distribution and electron transition process corresponding to the absorption of light with different photon energies by semiconductor materials. When the incident photon energy is very low, the incident photons interact with the electrons at the impurity energy levels of the semiconductor and excite the electrons to transition to the conduction band, thus generating free carriers. The advantage of this method is that it can realize bulk excitation of semiconductor materials, but this excitation method is affected by impurity concentration and energy level size, resulting in low carrier generation efficiency, which limits the improvement of the voltage conversion efficiency of PCSSs. When the incident photon energy is slightly lower than the bandgap of the semiconductor material, the electrons near the top of the semiconductor valence band can transition to the vicinity of the bottom of the conduction band under the combined action of photons and phonons. Without the dependence on impurities, the electron transition process in this case can occur more generally in the bulk of the material. In addition, since the electron transition process in this case is a multi-step process requiring phonon assistance, the absorption degree of the material to photons of this energy is improved to a certain extent but will not be completely absorbed in an extremely short distance. Therefore, this method can realize bulk excitation with a higher carrier concentration inside the material, which is conducive to improving the voltage conversion efficiency of PCSSs. When the incident photon energy is higher than the bandgap of the semiconductor material, electrons undergo direct interband transition under the action of photons with an extremely high transition probability. In this case, a large number of carriers can be generated in the material, but due to the strong light absorption of the material, carriers are only generated near the material surface, so this excitation method belongs to surface excitation and cannot effectively excite the PCSS to turn on. Phonon-assisted interband transition usually occurs in indirect bandgap semiconductor materials, but for direct bandgap semiconductor materials, electrons near the top of the valence band also have the opportunity to transition to the vicinity of the bottom of the conduction band under the combined action of photons with energy slightly lower than the bandgap and phonons, realizing phonon-assisted interband transition[37]. In contrast, Ga_2O_3 has a flatter valence band and richer phonon modes than other common direct bandgap semiconductor materials, which also provides a greater possibility for the occurrence of phonon-assisted interband transition inside it[38–40].

To verify the above physical process, variable-temperature photoluminescence (PL) measurements were carried out in the range of 80–300 K, and the temperature dependences of the PL intensity under 266 and 193 nm excitation were compared to elucidate the phonon-assisted electron transition process in the Ga_2O_3 crystal under 266 nm laser excitation. Figure 4(a) shows the optical bandgap and transmittance curves of the Ga_2O_3 crystal, where the optical bandgap is calculated based on the Tauc Plot method, and the results show that the optical bandgap of the Ga_2O_3 crystal is 4.69 eV. The photon energy corresponding to 266 nm light is about 4.66 eV, slightly less than the bandgap of the Ga_2O_3 crystal, and the photon energy corresponding to 193 nm light is about 6.42 eV, greater than the bandgap of the Ga_2O_3 crystal, which is just suitable for the verification experiment. It should be noted that the phonon-assisted process discussed in this work is more likely to occur within a limited sub-bandgap wavelength window close to the absorption edge. The 266 nm excitation used in this work is therefore a representative verification wavelength, rather than the only applicable wavelength for phonon-assisted excitation. The inset of Fig. 4(a) shows the transmittance of the Ga_2O_3 crystal, with a transmittance of 2.42% at 266 nm,

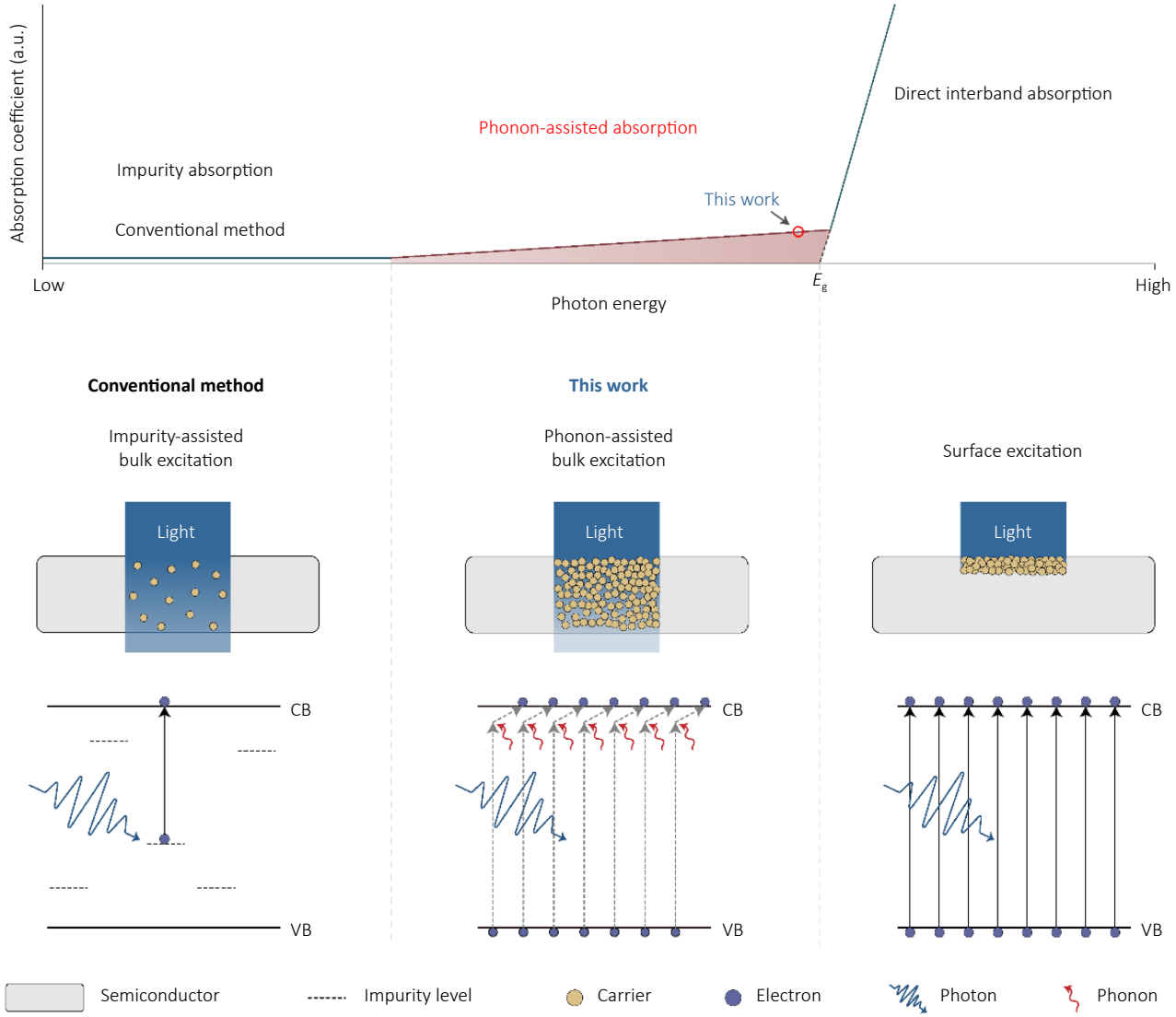


Fig. 3 | Light absorption, internal carrier excitation and electron transition processes of semiconductor materials under irradiation with light of different incident photon energies.

indicating that the Ga_2O_3 crystal with a thickness of 0.55 mm exhibits sufficient but incomplete absorption of 266 nm light. Ga_2O_3 is a direct bandgap semiconductor, in which the radiative recombination process does not require phonon participation and is not affected by temperature. Figure 4(b) and Figure S34 show the PL spectra of the Ga_2O_3 crystal excited by different excitation lasers at different temperatures, and their highly consistent line shapes also prove that the radiative recombination luminescence process in the Ga_2O_3 crystal is the same within the test temperature and excitation conditions of this study. Therefore, the different temperature dependences of the PL intensity under 266 and 193 nm excitation are mainly attributed to differences in the carrier excitation process, rather than to changes in the radiative recombination channel itself.

Figure 4(c) shows the variation trend of the PL intensity of the Ga_2O_3 crystal under 266 nm light excitation and the schematic diagram of its internal electron transition process, where the variable temperature PL spectra in the range of 80–300 K are shown in Fig. S35. The test results show that the luminescence intensity of the Ga_2O_3 crystal under 266 nm light excitation first increases and then decreases with the increase of temperature. The variation of PL intensity of semiconductor materials with temperature can usually be analyzed by the Arrhenius formula[41–43]:

$$I(T) = \frac{I_0}{A\exp\left(-\frac{E_b}{k_B T}\right) + 1}, \tag{1}$$

where I_0 is the initial luminescence intensity, A is a constant, E_b is the exciton binding energy, k_B is the Boltzmann constant, and T is the absolute temperature. The high

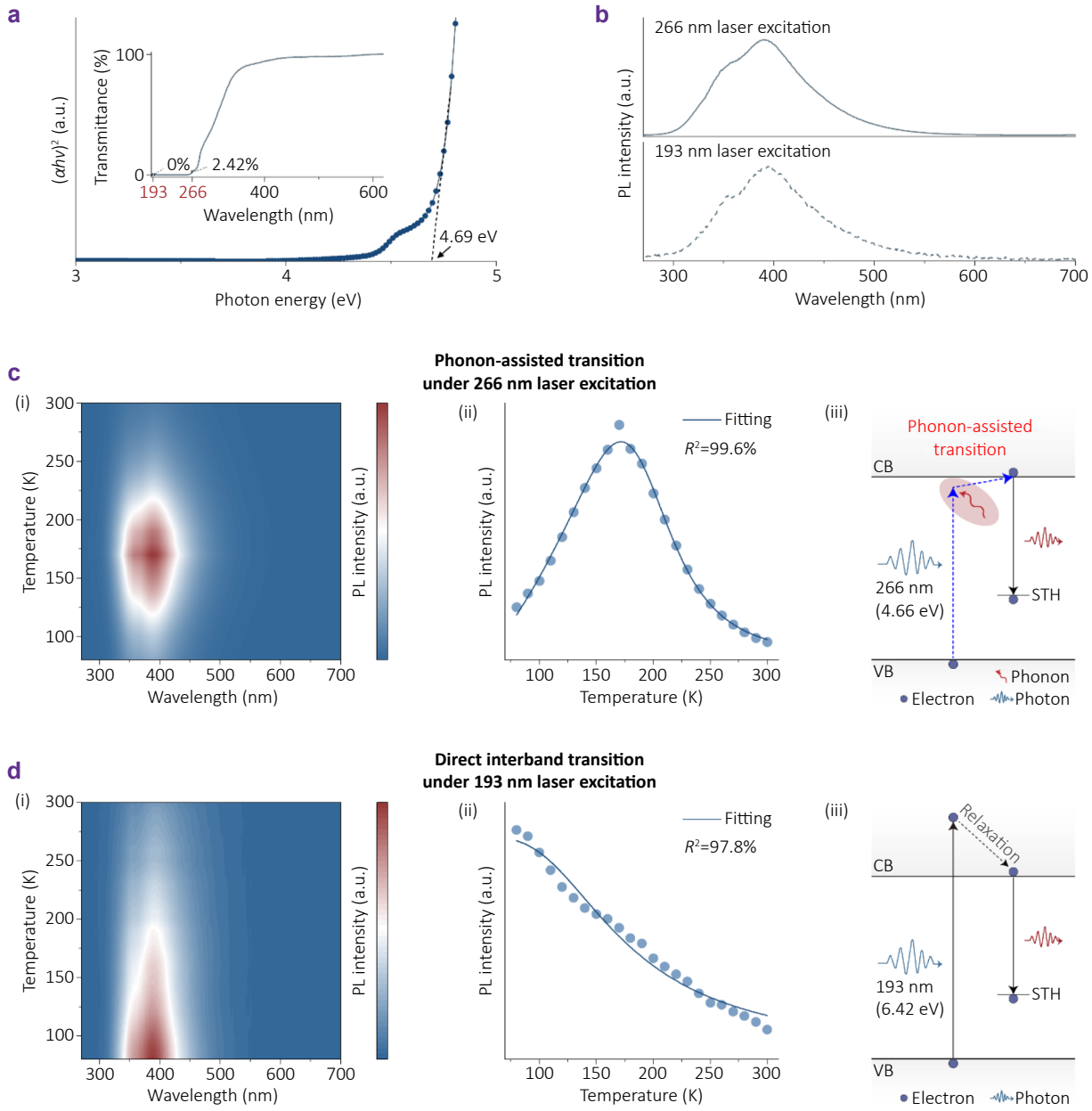


Fig. 4 | (a) Optical bandgap and transmittance of the Ga_2O_3 crystal. (b) PL spectra of the Ga_2O_3 crystal excited by 193 nm and 266 nm lasers at the same temperature. The high consistency indicates that the carrier recombination processes in the Ga_2O_3 crystal excited by the two different lasers are the same. (c) (i) Temperature-dependent mapping, (ii) variation of PL intensity with temperature, and (iii) phonon-assisted electron excitation and transition process of the Ga_2O_3 crystal under 266 nm laser. (d) (i) Temperature-dependent mapping, (ii) variation of PL intensity with temperature, and (iii) direct interband electron transition process of the Ga_2O_3 crystal under 193 nm laser.

mismatch of the fitting results indicates that the variation of the PL intensity of the Ga_2O_3 crystal under 266 nm light excitation does not conform to the Arrhenius model. This indicates the existence of an additional temperature-dependent process that dominates the carrier excitation efficiency in the Ga_2O_3 crystal. Considering that the photon energy of 266 nm light is slightly lower than the Ga_2O_3 bandgap, the interband excitation transition process of electrons in the Ga_2O_3 crystal under 266 nm light excitation requires phonons to provide additional energy and momentum, that is, the number of phonons will affect the probability of electron excitation transition. The number of phonons follows the Bose-Einstein statistical law and increases with the rise of temperature, thus improving the probability of phonon-assisted transition. Since the Ga_2O_3 crystal used cannot completely absorb 266 nm light, different transition probabilities will lead to changes in the initial number of excited electrons in the Ga_2O_3 crystal, thereby affecting the PL

intensity. Therefore, in addition to the Arrhenius formula, the temperature-dependent phonon number is also introduced into the Arrhenius model in this study to fit the PL intensity of the Ga_2O_3 crystal under 266 nm light excitation. The phonon number n_p is given by the Bose-Einstein statistics[40]:

$$n_p = \frac{1}{\exp\left(\frac{E_p}{k_B T}\right) - 1}, \tag{2}$$

where E_p is the phonon energy, k_B is the Boltzmann constant, and T is the absolute temperature. A high fitting goodness of 99.6% can prove that the model is consistent with the actual test results, that is, the interband excitation transition process of electrons in the Ga_2O_3 crystal under 266 nm light excitation is a phonon-assisted process. The non-monotonic evolution of the PL intensity can be attributed to the combined effect of two competing processes. With increasing temperature, the number of phonons increases, which enhances the probability of phonon-assisted excitation and thus raises the PL intensity. At higher temperatures, however, non-radiative recombination and thermal quenching gradually become dominant, resulting in a subsequent decrease in the PL intensity. Taking the electron excitation and recombination to the self-trapped hole (STH) energy level as an example[44], Fig. 4(c-iii) shows the schematic diagram of the electron excitation and recombination process in the Ga_2O_3 crystal under 266 nm light excitation. The photon energy of 266 nm light is slightly less than the bandgap, so under the excitation of 266 nm light, the electrons near the top of the valence band of the Ga_2O_3 crystal need the assistance of phonons to transition to the bottom of the conduction band, and then the electrons at the bottom of the conduction band move from the conduction band to the self-trapped hole (STH) energy level and emit photons. In the phonon-assisted light absorption process, the interband transition of electrons requires the combined action of both phonons and photons, and its transition probability is lower than that of the direct interband transition requiring only the action of photons, which provides theoretical support for realizing bulk excitation with a high carrier concentration inside Ga_2O_3 and thus achieving a high voltage conversion efficiency of the PCSS.

Figure 4(d) shows the variation trend of the PL intensity of the Ga_2O_3 crystal under 193 nm light excitation and the schematic diagram of its internal electron transition process, where the variable temperature PL spectra in the range of 80–300 K are shown in Fig. S36. It can be seen that the luminescence intensity of the Ga_2O_3 crystal decreases monotonically with the increase of temperature, and a fitting goodness of 97.8% indicates that the test results are highly consistent with the classical Arrhenius model. Considering that the photon energy of 193 nm light is much higher than the Ga_2O_3 bandgap, the electrons in Ga_2O_3 mainly undergo direct interband transition at this time, and the probability of their excitation transition is only determined by the photon energy and electron density of states, independent of temperature. The variation of its PL intensity is only caused by the influence of temperature on the luminescence intensity in the Arrhenius model, and the decrease of PL intensity with temperature is completely derived from the increase of non-radiative recombination probability caused by temperature rise, which is fully consistent with the intrinsic characteristics of direct interband transition. This behavior is clearly different from that under 266 nm excitation, where the carrier generation efficiency itself is additionally modulated by the temperature-dependent phonon number. Figure 4(d-iii) shows the electron excitation and recombination process in the Ga_2O_3 crystal under 193 nm light excitation. The photon energy of 193 nm light is greater than the bandgap, so under the excitation of 193 nm light, the electrons at the top of the valence band of the Ga_2O_3 crystal directly transition to the conduction band under the action of photons, and transition to the self-trapped hole (STH) energy level after relaxing to the bottom of the conduction band and emit photons. The above experiments prove that the Ga_2O_3 crystal has different absorption processes for light with different photon energies, and its absorption of 266 nm light is based on phonon-assisted light absorption, which verifies the scientificity and correctness of the phonon-assisted absorption mechanism proposed in this work.

3 Conclusions

Aiming at the voltage conversion bottleneck of traditional PCSSs caused by the dependence on extrinsic impurity absorption, this work proposes a novel operating mechanism of PCSSs based on phonon assistance, which fundamentally eliminates the dependence on impurity energy levels from the physical origin and solves the core problems of low carrier excitation efficiency, large on-state loss and narrow operating voltage range in the traditional mechanism. Based on this mechanism, Ga_2O_3 PCSS devices are fabricated using high-quality Fe-doped Ga_2O_3 single crystals. Under an excitation laser energy of 1.98 mJ and a bias electric field strength of 40 kV/cm, the device achieves a high voltage conversion efficiency of 98.93%, approaching the theoretical limit of 100%, a peak output power density of 17.7 MW/cm^2, and can maintain excellent voltage conversion efficiency over a wide bias voltage range of 50–4000 V. This work provides strong spectroscopic evidence for the phonon-assisted electron transition process in β-Ga_2O_3 through variable temperature spectroscopy experiments, thereby supporting the proposed mechanism for the performance breakthrough of the device. This work not only demonstrates leading overall performance among the reported β-Ga_2O_3 PCSSs, but also provides a new physical paradigm that may inspire the design of other PCSSs. After further studies and optimization of the intrinsic switching speed, thermal effects, long-term reliability, and practical applications of the Ga_2O_3 PCSS, it is expected to strongly

promote the development of HPM systems toward higher efficiency, higher power density, and lighter weight.

4 Experimental section

Material characterization: The Ga_2O_3 used in the experiment is high-resistivity Fe-doped Ga_2O_3. The X-ray diffraction (XRD) pattern and rocking curve of the Ga_2O_3 crystal sample are measured by an X-ray diffractometer (Rigaku SmartLab) to analyze the material structure and crystalline quality. The transmission electron microscopy (TEM) image of the Ga_2O_3 crystal sample is measured by a field emission transmission electron microscope (FEI Talos F200S) to analyze its microstructure. The Raman spectra data of the Ga_2O_3 crystal sample are measured by a micro-Raman confocal system (Horiba LabRam HR Evolution) with a 532 nm laser as the excitation light source to analyze its phonon vibration modes. The transmittance spectrum of the Ga_2O_3 crystal sample is measured by an ultraviolet-visible spectrophotometer to analyze its absorption and transmittance of light with different wavelengths. The variable temperature PL signals of the Ga_2O_3 crystal sample under 266 nm and 193 nm laser excitation are collected by a spectrometer (Ocean Optics QE65 Pro) to study its luminescent characteristics at different temperatures.

Device fabrication: A high-resistivity Fe-doped Ga_2O_3 bulk crystal with a size of 10.5 mm×10 mm×0.55 mm is selected. Rogowski metal electrodes with staggered positions are fabricated on two opposite surfaces of the Ga_2O_3 crystal through photolithography, electron beam evaporation, lift-off and other processes. The interface contact characteristics between the metal electrodes and the Ga_2O_3 crystal are then optimized by annealing in air at 400 °C for 30 min, thereby fabricating the Ga_2O_3 PCSS. The metal electrode adopts a Ti/Au/Ag/Au structure, and the shortest distance between the two Rogowski electrodes of the Ga_2O_3 PCSS is 1 mm.

Device testing: The Ga_2O_3 PCSS is packaged on a printed circuit board with impedance matching, and epoxy resin is coated around the Ga_2O_3 PCSS to prevent air breakdown. In the test, a high-voltage power supply charges a 10 nF high-voltage capacitor through a 10 MΩ resistor and provides a bias voltage for the Ga_2O_3 PCSS. The output end of the Ga_2O_3 PCSS is connected to an oscilloscope (50 Ω load, model: SIGLENT SDS5104X) through a coaxial attenuator with a nominal value of 60 dB. The trigger light source in the test system is a pulsed laser with a wavelength of 266 nm, with a spot diameter of about 1.5 mm, an incident frequency of 1 Hz and a pulse width of about 6 ns. The actual attenuation value of the attenuator with a nominal value of 60 dB used in the test system is determined through test calibration, with the test results shown in Fig. S37.

References

1. Huang X. The small-drone revolution is coming — scientists need to ensure it will be safe. *Nature* **637**, 29–30 (2025).
2. Wang YX, Sun G, Sun ZM et al. Toward realization of low-altitude economy networks: core architecture, integrated technologies, and future directions. *IEEE Trans Cognit Commun Networking* **11**, 2788–2820 (2025).
3. Ye L, Zhang J, Meng G. Research on defense-in-depth zone of low-altitude security area in nuclear power plant. *Nuclear Power Plants: Innovative Technologies for Instrumentation and Control Systems(Isnpp 2019)* **595**, 30–37 (2020).
4. Mao QD, Xiang ZW, Huang LY et al. High-power microwave pulse-induced failure on unmanned aerial vehicle system. *IEEE Trans Plasma Sci* **51**, 1885–1893 (2023).
5. Zhao M, Chen YZ, Zhou X et al. Investigation on falling and damage mechanisms of UAV illuminated by HPM pulses. *IEEE Trans Electromagn Compat* **64**, 1412–1422 (2022).
6. Huang J, Hu L, Yang XH et al. Modeling and simulation of Fe-doped GaN PCSS in high-power microwave. *IEEE Trans Electron Devices* **70**, 3489–3495 (2023).
7. Wu QL, Zhao YX, Xun T et al. Initial test of optoelectronic high power microwave generation from 6H-SiC photoconductive switch. *IEEE Electron Device Lett* **40**, 1167–1170 (2019).
8. Yang XH, Hu L, Liu JL et al. Si_3N_4 passivation and side illumination of high-power photoconductive semiconductor switch based on free-standing SI-GaN. *IEEE Trans Electron Devices* **70**, 1128–1133 (2023).
9. Wei JH, Li S, Wang LN et al. Properties of switching transient in the semi-insulating GaAs photoconductive semiconductor switch with opposed contacts. *IEEE Trans Plasma Sci* **50**, 3635–3643 (2022).
10. Xu M, Dong HT, Liu C et al. Investigation of an opposed-contact GaAs photoconductive semiconductor switch at 1-kHz excitation. *IEEE Trans Electron Devices* **68**, 2355–2359 (2021).
11. Yu HB, Memon MH, Yao MJ et al. A miniaturized cascaded-diode-array spectral imager. *Nat Photonics* **19**, 1322–1329 (2025).
12. Luo YM, Yu HB, Wang DH et al. A single diode with integrated photosensing, memory and processing for neuromorphic image sensors. *Nat Electron* **9**, 404–413 (2026).
13. Chen S, Wu XH, Fu CJ. Active tuning of anisotropic phonon polaritons in natural van der Waals crystals with negative permittivity substrates and its application in energy transport. *Opto-Electron Sci* **3**, 240002 (2024).
14. Zhu SQ, Zhang X, Liu SY et al. 8-inch nano-polycrystalline hBN for neutron radiography. *PhotoniX* **7**, 1 (2026).
15. Zheng CL, Ni PN, Xie YY et al. On-chip light control of semiconductor optoelectronic devices using integrated metasurfaces. *Opto-Electron Adv* **8**, 240159 (2025).
16. Chiang JL, Yadlapalli BK, Chen MI et al. A review on gallium oxide materials from solution processes. *Nanomaterials* **12**, 3601 (2022).
17. Xiao YM, Xu YK, Chen JL et al. Advancements in direct nitridation of aluminum method for AlN crystal growth. *Phys Status Solidi A* **222**, 2400734 (2024).
18. Zhang X, Xu MF, Ng ZK et al. Diamond: recent progress in synthesis and its potential in electronics. *Chem Mater* **37**, 2679–2698 (2025).
19. Pearton SJ, Yang JC, Cary IV PH et al. A review of Ga_2O_3 materials, processing, and devices. *Appl Phys Rev* **5**, 011301 (2018).
20. Zhang JC, Dong PF, Dang K et al. Ultra-wide bandgap semiconductor Ga_2O_3 power diodes. *Nat Commun* **13**, 3900 (2022).
21. Xu JJ, Zheng W, Huang F. Gallium oxide solar-blind ultraviolet photodetectors: a review. *J Mater Chem C* **7**, 8753–8770 (2019).
22. Zhang JS, Kuang XX, Tu R et al. A review on synthesis and applications of gallium oxide materials. *Adv Colloid Interface Sci* **328**, 103175 (2024).
23. Zhou H, Zhang JC, Zhang CF et al. A review of the most recent progresses of state-of-art gallium oxide power devices. *J Semicond* **40**,

011803 (2019).
24. Dowling KM, Chatterjee B, Ghandiparsi S et al. Evaluation of Fe-βGa_2O_3 for photoconductive semiconductor switching. *IEEE Trans Electron Devices* **71**, 1535–1540 (2024).
25. Shen TJ, Wang LN, He T et al. Test on the output characteristics of Fe-β-Ga_2O_3 photoconductive semiconductor device toward high-power microwave sources. *IEEE Trans Electron Devices* **72**, 3638–3645 (2025).
26. Xu K, Chen ZP, Lin ZY et al. Preliminary development and high-voltage lifetime testing of vertical photoconductive semiconductor switches based on Fe-doped β-Ga_2O_3. *High Power Laser Part Beams* **37**, 065004 (2025).
27. Pavlidis S, Medwig G, Thomas M. Ultrawide-bandgap semiconductors for high-frequency devices. *IEEE Microw Mag* **25**, 68–79 (2024).
28. Tsao JY, Chowdhury S, Hollis MA et al. Ultrawide-bandgap semiconductors: research opportunities and challenges. *Adv Electron Mater* **4**, 1600501 (2018).
29. Jia LM, Cheng L, Zheng W. 8-nm narrowband photodetection in diamonds. *Opto-Electron Sci* **2**, 230010 (2023).
30. Fu JC, Jiang MT, Wang Z et al. Supercritical metalens at h-line for high-resolution direct laser writing. *Opto-Electron Sci* **3**, 230035 (2024).
31. Meyers V, Voss L, Flicker JD et al. Photoconductive semiconductor switches: materials, physics, and applications. *Appl Sci* **15**, 645 (2025).
32. Wang Z, Zhang LX, Duan KK et al. Ultra-high withstand voltage (>120 kV cm^{-1}) sub-nanosecond (<0.5 ns) aluminum nitride photoconductive semiconductor switch. *Chin Sci Bull* **71**, 2035–2043 (2026).
33. Han ZR, Lee J, Mazumder A et al. Record performance in intrinsic, impurity-free lateral diamond photoconductive semiconductor switches. *Appl Phys Lett* **126**, 152105 (2025).
34. Wei Y, Zhang ZC, Xu C et al. Correlating the electronic structures of β-Ga_2O_3 to its crystal tilts induced defects at nanoscale. *Mater Today Phys* **46**, 101518 (2024).
35. Zhang NJ, Lin ZG, Wang Z et al. Under-seawater immersion β-Ga_2O_3 solar-blind ultraviolet imaging photodetector with high photo-to-dark current ratio and fast response. *ACS Nano* **18**, 652–661 (2024).
36. Zeng LL, Wang LN, Niu XY et al. Characteristics comparison of SiC and GaN extrinsic vertical photoconductive switches. *IEEE J Electron Devices Soc* **12**, 249–255 (2024).
37. Dumke WP. Indirect transitions at the center of the brillouin zone with application to InSb, and a possible new effect. *Phys Rev* **108**, 1419–1425 (1957).
38. Mock A, Korlacki R, Briley C et al. Band-to-band transitions, selection rules, effective mass, and excitonic contributions in monoclinic β−Ga_2O_3. *Phys Rev B* **96**, 245205 (2017).
39. Cheng L, Wu YL, Zhong WB et al. Photophysics of β-Ga_2O_3: phonon polaritons, exciton polaritons, free-carrier absorption, and band-edge absorption. *J Appl Phys* **132**, 185704 (2022).
40. Cheng L, Zhu YM, Wang WL et al. Strong electron-phonon coupling in β-Ga_2O_3: a huge broadening of self-trapped exciton emission and a significant red shift of the direct bandgap. *J Phys Chem Lett* **13**, 3053–3058 (2022).
41. Cheng L, Zheng W. Exciton thermodynamics in pure diamond. *Laser Photonics Rev* **19**, 2400935 (2025).
42. As'ham K, Berhe AM, Al-Ani IAM et al. Recent advances in exciton-polariton in perovskite. *Opto-Electron Sci* **4**, 250001 (2025).
43. Krustok J, Collan H, Hjelt K. Does the low-temperature Arrhenius plot of the photoluminescence intensity in CdTe point towards an erroneous activation energy. *J Appl Phys* **81**, 1442–1445 (1997).
44. Ho QD, Frauenheim T, Deák P. Origin of photoluminescence in β−Ga_2O_3. *Phys Rev B* **97**, 115163 (2018).

Acknowledgements

This work was financially supported by the National Natural Science Foundation of China (No. 62374186).

Author contributions

All authors commented on the manuscript.
Conceptualization: Wei Zheng
Methodology: Wei Zheng, Zhao Wang, Lixin Zhang, Zhan Sui
Investigation: Zhao Wang, Lixin Zhang, Lu Cheng, Naiji Zhang, Danwen Zhang, Xin Zhang, Yu Lu
Visualization: Zhao Wang
Supervision: Wei Zheng
Resources: Wei Zheng, Hongji Qi, Duanyang Chen
Funding acquisition: Wei Zheng
Writing—original draft: Zhao Wang
Writing—review & editing: Wei Zheng

Competing interests

The authors declare no competing financial interests.

Supplementary information

Supplementary information for this paper is available at
https://doi.org/10.29026/oes.2026.260011

Open Access This article is licensed under a Creative Commons Attribution 4.0 International License, which permits use, sharing, adaptation, distribution and reproduction in any medium or format, as long as you give appropriate credit to the original author(s) and the source, provide a link to the Creative Commons license, and indicate if changes were made. To view a copy of this license, visit http://creativecommons.org/licenses/by/4.0/
©The Author(s) 2026.
Published by Editorial Office of *Opto-Electronic Science*, Institute of Optics and Electronics, Chinese Academy of Sciences.

Opto-Electronic Journals Group
www.oejournal.org
Scan for Article PDF